Sustainable Energy & Fuels

ROYAL SOCIETY OF CHEMISTRY

PAPER

View Article Online
View Journal | View Issue

Cite this: *Sustainable Energy Fuels*, 2026, **10**, 2021

Selective oxidation of polyolefins to carbon monoxide by photo-assisted catalysts

Hiroki Nagai, Hiroaki Kaneko, Yohei Cho, Akira Yamaguchi and Masahiro Miyauchi *

Polyolefins are produced in vast quantities, yet their degradation and recycling remain challenging due to their inherent chemical inertness. One of the conventional recycling approaches is the gasification process, which generates hydrogen (H_2) and/or carbon monoxide (CO) from plastic waste by high temperature treatment. However, its large energy consumption and poor product gas selectivity hinder practical applications. This study uses photon energy to promote the gasification of polyolefins through bandgap-driven and/or photothermal processes. We investigated the difference in CO production selectivity and underlying reaction mechanisms using rhodium-loaded strontium titanate ($Rh/SrTiO_3$) and rhodium-loaded mesoporous silica (Rh/MCM-41) as photo-assisted catalysts under ultraviolet light irradiation. The $Rh/SrTiO_3$ is capable of bandgap excitation in addition to the photothermal effect, while the Rh/MCM-41 only causes the photothermal effect because of the ultra-widegap nature of silica. Activity results of *n*-octane revealed that Rh/MCM-41 exhibited markedly higher CO production selectivity than $Rh/SrTiO_3$. Liquid-phase analysis of *n*-octane on intermediate species indicates that the high selectivity originates from the milder oxidation power provided by Rh/MCM-41. These findings demonstrate that photothermal effects possess inherently higher selectivity toward polyolefin gasification into CO compared to a reaction by bandgap excitation, owing to the mild oxidation process in the photothermal Rh/MCM-41 system. Overall, the present results offer valuable insights for designing selective and energy-efficient strategies for polyolefin gasification utilizing photon energy.

Received 11th January 2026
Accepted 14th March 2026

DOI: 10.1039/d6se00038j

rsc.li/sustainable-energy

1. Introduction

Plastics are used in vast quantities worldwide today. While various plastics are used globally, low-density polyethylene (LDPE), high-density polyethylene (HDPE), and polypropylene (PP) are particularly prevalent types of plastic.[1] These three polyolefins account for half of total plastic production, making their effective utilization critically important for a sustainable society.[2] On the other hand, the degradation of these polyolefins is extremely difficult because of their inert C–C and C–H bonds.[2] Due to their chemical inertness, conventional polyolefin recycling has primarily focused on producing liquid fuels and chemicals through pyrolysis.[3–8] However, recycling through pyrolysis requires high-temperature conditions, and the high temperatures tend to result in low selectivity of the products. Therefore, the decomposition of LDPE or HDPE by the pyrolysis process yields limited products with low qualities, which has been a barrier preventing commercial pyrolysis from being widely adopted.[1,9]

To address this selectivity issue, an approach involving plastic gasification has been reported.[10–12] The advantage of plastic gasification lies in the ability to synthesize energy sources and/or valuable chemicals from the resulting gases, such as the mixture of hydrogen (H_2) and carbon monoxide (CO), called syngas. Recently, pilot-scale gasification systems have been demonstrated,[13] however, these systems require quite high temperature of 800 to 1500 °C. In addition to the high operating temperature, the selective reaction for the specific target product is quite difficult to proceed. In air gasification, which utilizes atmospheric oxygen for oxidative gasification, carbon dioxide (CO_2) emission is caused by the oxidation of plastics. Besides CO_2 emission, minor byproducts such as tar and hydrocarbons also cause problems like clogged piping.[13] In steam gasification, which uses steam to modify plastics, the reaction is endothermic and requires energy for heating and also causes CO_2 emission.[14,15] To make gasification practical, several approaches have been attempted,[16–18] however, their practical implementation is quite challenging due to the high temperatures and complex catalytic reactions involved.[19]

While pyrolysis and thermal gasification require such harsh conditions of high temperature and pressure, the photo-assisted process utilizes renewable energy like sunlight, allowing reactions to proceed under relatively mild conditions. Furthermore, these mild conditions are expected to enable high selectivity under precise control.[20] The previous studies reported photocatalytic degradations using aqueous dispersion systems, which targeted microplastics in water,[21–27] and film systems.[28–31] However, the aim

Department of Materials Science and Engineering, School of Materials and Chemical Technology, Institute of Science Tokyo, 2-12-1 Ookayama, Meguro-ku, Tokyo 152-8552, Japan. E-mail: mmiyauchi@ceram.titech.ac.jp

of these studies was just the degradation of plastics into CO_2 or the production of H_2 through water splitting, where plastic wastes acted as sacrificial agents for oxidation reactions.[32,33] A limited number of studies have quantitatively reported CO production during photocatalytic degradation of polyolefins. For example, Ohtani *et al.* reported the CO production by the light irradiation to LDPE films mixed with TiO_2.[34] In addition to these reports, researches on photothermal plastic decomposition have been actively pursued in recent years,[35–39] and the target products of these researches were H_2, liquid alkanes, or waxes. In addition to these target products, syngas production involving CO is highly expected, since syngas can be converted into valuable multi-carbon chemicals by the Fischer–Tropsch process under relatively mild conditions.[40]

This study focuses on CO generation from LDPE plastics and compares the CO/CO_2 ratios in the produced gases between two photo-assisted catalyst systems under ultraviolet (UV) light irradiation. While previous studies reported gasification of polyolefins, the influence of different light-response mechanisms on CO/CO_2 selectivity has not been compared. In this study, one catalyst is rhodium-loaded strontium titanate ($Rh/SrTiO_3$), and another is rhodium-loaded silica (Rh/MCM-41). We choose the Rh as a promoter for both systems[40] and it also causes a surface heating by plasmonic absorption in Rh. As a Rh catalyst support, we choose $SrTiO_3$, since it is a well-known photocatalyst with strong oxidation power by photogenerated holes through the bandgap excitation,[41] and it demonstrated light-driven oxidation of simple hydrocarbons such as methane, indicating that $SrTiO_3$ is a suitable platform for hydrocarbon valorization under light irradiation. Further, Rh nanoparticles on $SrTiO_3$ can also cause a photothermal effect.[42,43] As another catalyst support, we use MCM-41, which only causes photothermal effect under UV irradiation because of the ultra-widegap nature of silica. Indeed, the previous study reported that the Rh/MCM-41 cleaved C–H bonds by a thermocatalytic effect in Rh,[44] thus, it is expected that the photothermal effect promotes the gasification of LDPE under UV irradiation. In the present study, we first investigate the produced CO/CO_2 ratio as the selectivity factor using liquid *n*-octane (C_8H_{18}) as a model substance for polyolefins to simplify the reaction system, and for discuss the reaction mechanism for the bandgap excitation process and photothermal process by monitoring intermediate species in these reactions. C_8H_{18} offers a distinct advantage in enabling liquid-phase analysis by GC-MS. This approach allows direct identification of reaction intermediates and has not been employed in previous studies. Based on these examinations, we extended our investigation to the CO generation from LDPE, which will provide mechanistic insights for syngas generation from plastics.

2. Experimental section

2.1. Materials

n-Octane (C_8H_{18}) as a model substance for LDPE was purchased from Kanto Chemical. The strontium titanate ($SrTiO_3$) powder was purchased from Sigma-Aldrich, and tetraethoxysilane (TEOS), cetyltrimethylammonium bromide (CTAB), aqueous ammonia (NH_3 aq), and ethanol (dehydrated) were purchased from Kanto Chemical. Rhodium(III) chloride ($RhCl_3$) was also purchased from Kanto Chemical. Mesoporous silica (MCM-41 and SBA-15) was purchased from Sigma-Aldrich. LDPE powder was also obtained from Sigma-Aldrich (average M_w ~4000 by GPC, average M_n ~1700 by GPC).

2.2. Synthesis of catalysts

$Rh/SrTiO_3$ was synthesized *via* an impregnation method. Commercial $SrTiO_3$ powder was dispersed in 40 mL of deionized water, followed by the addition of an aqueous rhodium trichloride ($RhCl_3$) solution corresponding to 1 wt% Rh relative to $SrTiO_3$. The amount of Rh was set to 1 wt% to match the conditions of Rh/MCM-41. The $RhCl_3$ stock solution was prepared at a concentration of 1 g-Rh L^{-1}, and 1.5 mL of this solution was added to the solution containing 150 mg $SrTiO_3$. The mixture was dried overnight to obtain $RhO_x/SrTiO_3$, which was subsequently reduced under 1 vol% H_2/Ar atmosphere to yield $Rh/SrTiO_3$. Reduction was performed by heating from room temperature at 10 °C min^{-1}, holding at 450 °C for 2 hours, and then allowing natural cooling to room temperature. During this process, the reducing gas was continuously purged at 50 mL min^{-1} until the system cooled sufficiently.

Rh/MCM-41 was synthesized *via* a soft template method, similar to the previous report.[44] Hexadecyltrimethyl-ammonium bromide, rhodium(III) chloride, tetraethyl silane, and deionized water were mixed and hydrolysed overnight. The resulting mixture was dried overnight, followed by calcination at 550 °C for 4 hours to remove organic species. Finally, the sample was reduced under the same condition as $Rh/SrTiO_3$ We also prepared Rh-loaded mesoporous silica using commercial MCM-41 and SBA-15 materials (denoted as [COM] Rh/MCM-41 and [COM]Rh/SBA-15) by the same impregnation method described above. Instead of $SrTiO_3$, 150 mg of commercial MCM-41 or commercial SBA-15 was used as support materials.

2.3. Characterization

The X-ray diffraction (XRD) patterns of the samples were measured using Rigaku, MiniFlex 600C. The scanning electron microscope (SEM) images of the samples were taken using JEOL, JCM-7000 NeoScopeTM. The transmission electron microscope (TEM) images of the samples were taken using JEOL, JEM-2100F. UV-visible (UV-vis) absorption spectra were recorded using JASCO, V-770 with a diffuse reflectance method. The isotherm and surface areas of powder catalysts were measured by a Brunauer–Emmett–Teller (BET) method[45] using MICROMERITICS, TriStar II.

2.4. Activity measurement

Fig. S1 in SI shows the schematic illustration of the reactor for the degradation of C_8H_{18}. A total of 16 mg of catalyst powder was dispersed in 1.5 mL of C_8H_{18}, and either pure oxygen (O_2) or a mixed gas of O_2 and nitrogen (N_2) was purged into the system for more than 5 min. The reactor consisted of a quartz cell with 1 cm sides as shown in Fig. S1 in SI. The mixture was then irradiated with a mercury–xenon (Hg–Xe) lamp at a distance of 2.5 cm. The light source was HAYASHI-REPIC LA-410UV-5, and

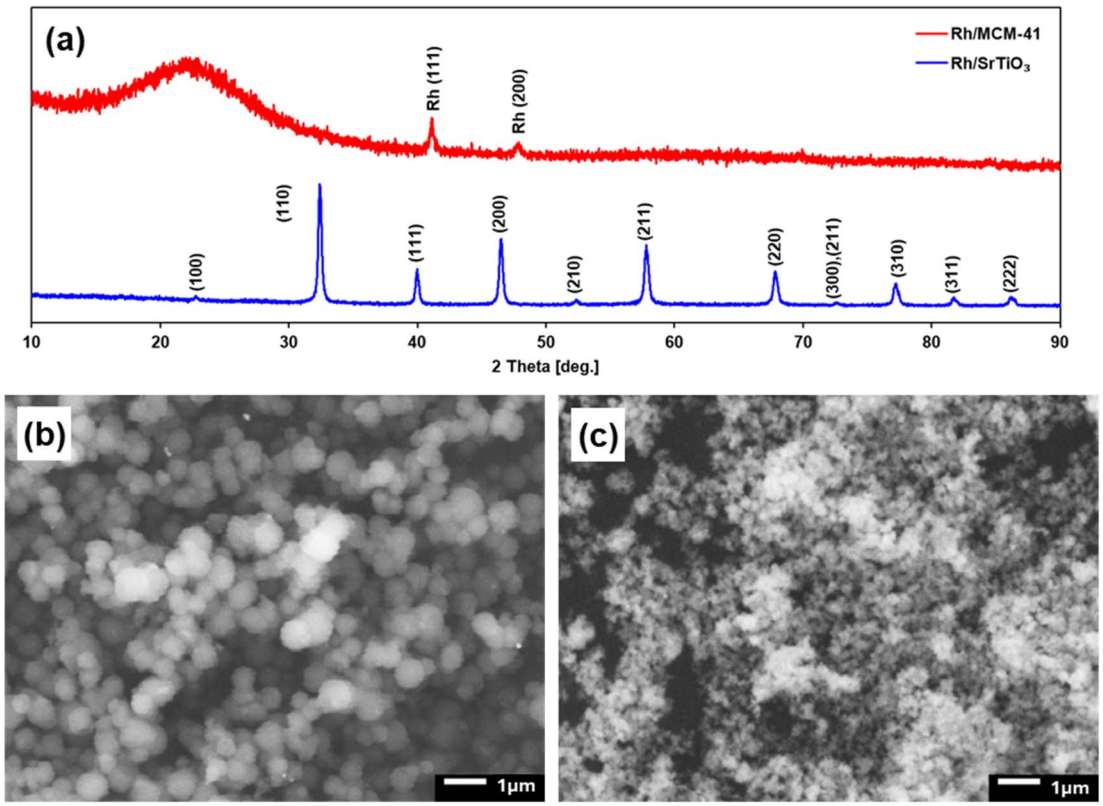

Fig. 1 (a) XRD patterns, (b) SEM image of Rh/MCM-41, and (c) SEM image of Rh/$SrTiO_3$.

wavelengths longer than 275 nm were irradiated using a short-cutoff filter. During the experiment, the suspension was continuously stirred at 400 rpm using a magnetic stirrer. After 3 hours of light irradiation, the headspace gases were analysed using a gas chromatography (GC-BID; SHIMADZU, Tracera), and the liquid products were analysed by a gas chromatography-mass spectrometry (GC-MS; SHIMADZU, GCMS-QP2010 Ultra). The liquid products were sampled with a micro-syringe and injected into the sample evaporation chamber equipped in the GC-MS apparatus. The injected samples were subsequently evaporated and analysed in the gas phase.

LDPE degradation experiments were conducted using a similar reactor system to the *n*-octane degradation experiment. Fig. S2 in SI presents the schematic illustration for LDPE degradation. A mixture of 7.0 mg of LDPE powder (corresponding to 1.0 mmol of CH_2 units) and 5.0 mg of [Com] Rh/MCM-41 or Rh/$SrTiO_3$ was ground in an agate mortar and placed into a porous ceramic cup. The cup was placed into a quartz cell and purged with dried air containing a negligible amount of CO_2. The sample was then irradiated by UV light at a distance of 2.5 cm using the same light source as in the experiment of C_8H_{18} degradation. After 24 hours of irradiation, the headspace gases were analysed using GC-BID.

3. Results and discussion

3.1. Characterization and physical properties of catalysts

Fig. 1a shows X-ray diffraction patterns of Rh/MCM-41 and Rh/$SrTiO_3$. Rh/MCM-41 exhibits a broad peak corresponding to amorphous SiO_2 along with diffraction peaks attributed to the metallic Rh. Rh/$SrTiO_3$ showed sharp peaks of $SrTiO_3$, while Rh peaks were not obvious due to the strong peak intensity of the $SrTiO_3$. Fig. 1b and c show SEM images of Rh/MCM-41 and Rh/$SrTiO_3$, respectively. The particle size of Rh/MCM-41 was considerably larger than that of Rh/$SrTiO_3$, and both samples exhibited spherical morphologies. Fig. S3a–c in SI show TEM images of the synthesized Rh/MCM-41. These images were observed for the sample prepared by an ion slicer, which cut individual particles into slices, enabling observation of their internal cross-sectional pore structures. The striped contrast pattern is visible, which is interpreted as the mesoporous framework. The pore diameter appears to be approximately 5 nm, and the pores extend radially from the particle center toward the outer surface. Dark spots correspond to Rh metal nanoparticles, which are uniformly dispersed throughout the particle. The energy-dispersive X-ray spectroscopy (EDS) results shown in SI (Fig. S4) revealed that dark spots consist of Rh. Fig. S5 in SI shows TEM images of commercial Rh/MCM-41. Similar to the lab-fabricated Rh/MCM-41, the striped mesoporous contrast was clearly observed. In both mesoporous silica samples, Rh nanoparticles were found to align along the mesopore channels. Also, Rh nanoparticles were existed on the surface of silica particles, where the liquid C_8H_{18} and the solid LDPE as model plastic substances can be accessed to the Rh particles in our photo-assisted degradation tests. Fig. S3d and e in SI show the TEM images of Rh/$SrTiO_3$. The particle size of Rh on $SrTiO_3$ was almost the same as those on silica samples. Based on previous XPS analysis of Rh/$SrTiO_3$ prepared under

Table 1 Surface area of each catalyst

Catalyst	Surface area [$m^2\ g^{-1}$]
Rh/MCM-41	988
$Rh/SrTiO_{3ct}$	19.4

the similar conditions,[42] the supported Rh species are considered to be predominantly metallic (Rh^0) after the reduction process.

Fig. S6a in SI presents the N_2 adsorption–desorption isotherm of Rh/MCM-41, which exhibited a type IV isotherm, indicating the presence of mesopores. Fig. S6b in SI shows the pore size distribution of Rh/MCM-41, where the pore diameter was mainly distributed between 5 and 7 nm. Table 1 summarizes the surface areas of the catalysts. Rh/MCM-41 exhibited a significantly large surface area owing to its mesopore structure.

Fig. 2 shows the UV-vis absorption spectra of $Rh/SrTiO_3$ and Rh/MCM-41. $Rh/SrTiO_3$ exhibited the bandgap absorption in the range of 300–400 nm, whereas Rh/MCM-41 did not show such steep absorption within the UV-vis region. Because the spectra were collected in diffuse reflectance mode, the baseline features at longer wavelengths may be affected by differences in scattering behavior and optical properties of the powder supports. Nevertheless, a broad absorption attributable to Rh nanoparticles was observed in both spectra.

3.2. *n*-Octane degradation

We measured the liquid C_8H_{18} temperatures of each catalyst under UV irradiation using a thermocouple. Table S1a in SI summarizes the temperature results. The temperatures of both catalysts under UV irradiation were not so different (~60 °C).

Fig. 3a and b show the amounts of gaseous products generated from the degradation of C_8H_{18} under the different O_2 concentration conditions with UV light irradiation. Control experiments of C_8H_{18} degradation were also conducted under UV irradiation without catalysts, as well as under dark conditions with heating at 60 °C, but the product amounts were negligible as compared to the case using catalysts and lights (Fig. S7 in SI). As shown in Fig. 3, the trends in gas products differed significantly between the two catalysts. Rh/MCM-41 exhibited high yields of CO, C_2H_4, and C_2H_6 production under low O_2 concentrations, and the amounts of these products remained nearly constant as the O_2 concentration increased. In contrast, the amount of CO_2 increased with increasing O_2 concentration. $Rh/SrTiO_3$ produced a larger total amount of gaseous products, but CO_2 was the predominant product. Notably, at low O_2 concentrations, only trace amounts of CO, C_2H_4, and C_2H_6 were detected in the case of $Rh/SrTiO_3$. We also investigated the optimum loading amount of Rh on mesoporous silica for CO production, and the optimum amount was 1% (see our SI, Fig. S8). Hereafter, we used 1% Rh-loaded catalysts for our further study.

Fig. 3c presents the CO/CO_2 ratio calculated from the data of Fig. 3a and b, clearly highlighting the difference between Rh/MCM-41 and $Rh/SrTiO_3$. Rh/MCM-41 exhibited superior CO production selectivity, particularly under low O_2 conditions. We also investigated the catalytic activities for the Rh-loaded mesoporous SiO_2 samples, which were prepared using a commercial MCM-41 and SBA-15 (Fig. S9 in SI). The overall product selectivity trends were not different in these silica samples.

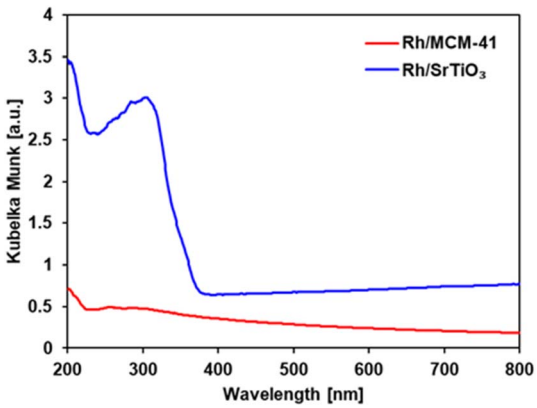

Fig. 2 UV-vis absorption spectra.

3.3. Mechanism study

We investigated the intermediate species in C_8H_{18} under UV irradiation by GC-MS, and the results are shown in Fig. 4. Detailed mass spectra are also shown in Fig. S10. Based on these results, the identified compounds were classified into three groups: the peaks appearing at 11–12.8 min were assigned to 2-octanone, 3-octanone, and 4-octanone, those at 12.8–16 min to 2-, 3-, and 4-octanol, and those at 17–19 min to ethers. Rh/MCM-41 predominantly produced alcohol-type compounds, whereas $Rh/SrTiO_3$ mainly yielded ketone-type products. In general, alcohols are formed under relatively reductive conditions, while ketones are generated under oxidative conditions.[46] Therefore, these results suggest that Rh/MCM-41 provides a milder oxidative power for the oxidation of C_8H_{18}. This observation is consistent with the well-known behavior of photocatalysts that are capable of bandgap excitation, such as $SrTiO_3$, which degrade polyolefins through the direct oxidation by photogenerated holes and/or reactive oxygen species (ROS). Because photogenerated holes and ROS possess strong oxidizing power, polyolefins tend to be fully oxidized to CO_2.[47] In contrast, Rh/MCM-41 provides a milder power compared to $Rh/SrTiO_3$.

Next, we discuss the role of light absorption by Rh nanoparticles and their interaction with the support. Unlike typical plasmonic metals such as gold or silver, Rh nanoparticles exhibit plasmonic absorption mainly in the UV region. Previous studies reported that photothermal heating in Rh nanoparticles was predominantly induced by interband electronic transitions rather than localized surface plasmon resonance.[48] The absorbed photon energy is rapidly dissipated as heat through electron–phonon coupling, leading to localized temperature increases at the Rh nanoparticle surface. Importantly, the

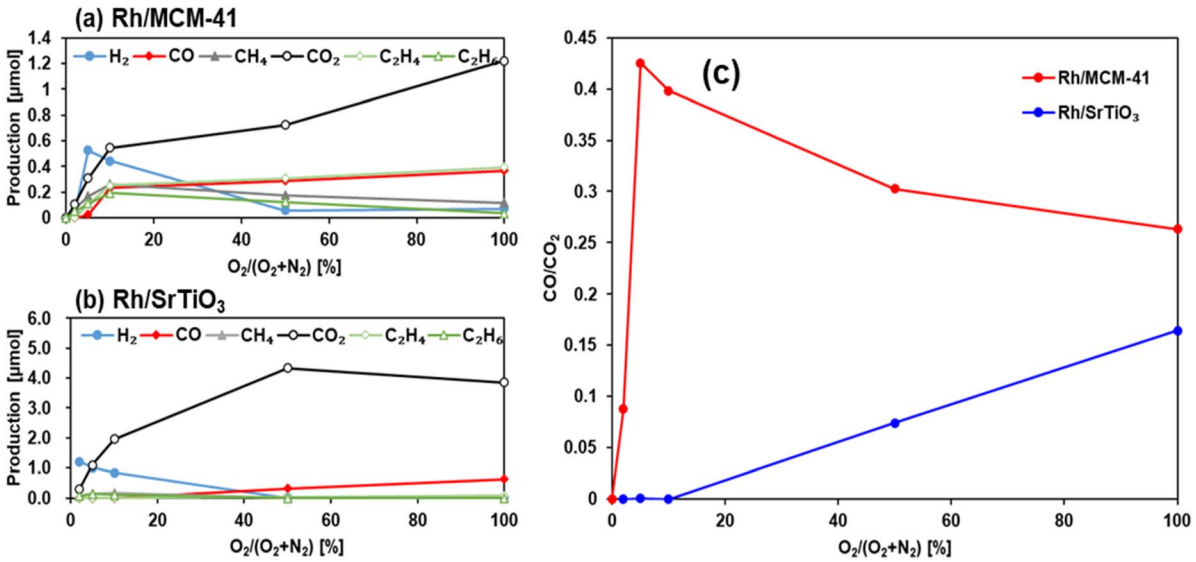

Fig. 3 (a) and (b) The amount of gas produced by C_8H_{18} degradation and (c) CO/CO_2 ratio under UV irradiation.

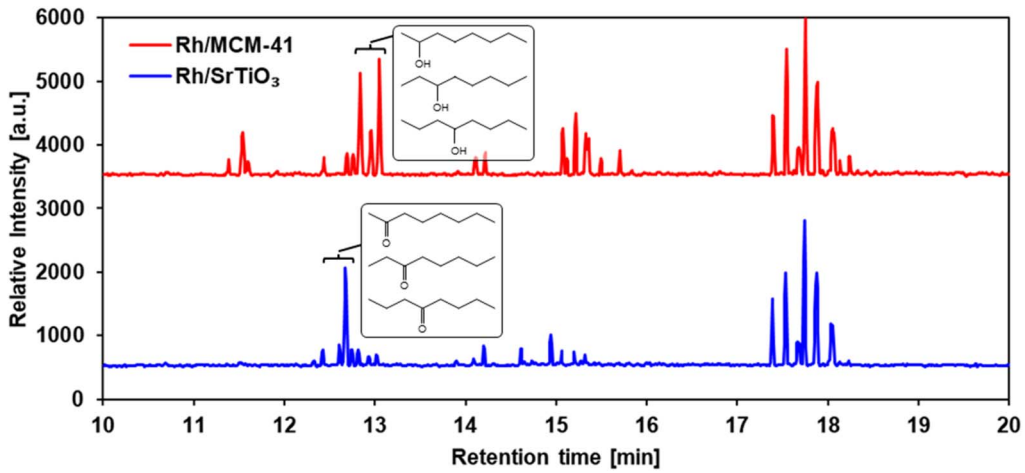

Fig. 4 Liquid products analysed by GC-MS. The peaks from 11 to 12.8 min were identified as ketone group, the peaks from 12.9 to 16 min were identified as alcohol group, and the peaks from 17 to 19 min were identified as ether group.

interaction between Rh nanoparticles and the support plays a crucial role in determining the reaction pathway. In the Rh/MCM-41 system, the inert and wide-bandgap silica support does not participate in photoinduced charge transfer, resulting in a predominantly thermal activation of surface reactions. In contrast, in the $Rh/SrTiO_3$ system, photoexcitation of the semiconductor support can generate charge carriers that interact with Rh nanoparticles, promoting oxidative pathways and thereby lowering CO selectivity.

We also investigated the light intensity dependence on the product amounts for each catalyst, and the results are shown in Fig. S11 in SI. In the case of Rh/MCM-41, the product amounts did not show a linear dependence on light intensity. In contrast, $Rh/SrTiO_3$ showed an approximately linear increase in CO_2 and CO production with increasing light intensity. These contrasting behaviors suggest different roles of light in the two systems. In the case of $Rh/SrTiO_3$, the reaction rate would depend on the number of absorbed photons in $SrTiO_3$ under the photocatalytic process. In contrast, the non-linear response of Rh/MCM-41 is owing to other factors, such as the surface temperature and/or the thermocatalytic activation process. The action spectrum result of the $Rh/SrTiO_3$ also indicates the bandgap excitation boosts the degradation of hydrocarbons (Fig. S12 in SI).

3.4. LDPE degradation

Finally, LDPE degradation tests were conducted using a closed quartz cell as shown in our SI (Fig. S2). During the UV light irradiation, LDPE was melted by heat generation under light irradiation, because the surface temperatures of catalysts were increased over 140 °C as shown in Table S1b in SI. Fig. 5 shows the produced gas amount by LDPE degradation. Although the control experiment under Ar atmosphere without catalyst

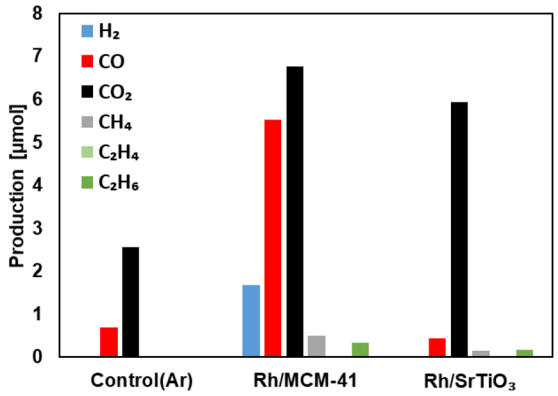

Fig. 5 Amount of produced gas by LDPE degradation under UV light irradiation. O_2/N_2 = 21%:79% (dried air). Control test was conducted under Ar atmosphere.

exhibited the small amount of CO and CO_2 generation under UV irradiation, the addition of catalysts promoted the LDPE degradation. Interestingly, the Rh/MCM-41 exhibited higher CO selectivity, whereas the Rh/$SrTiO_3$ dominantly produced CO_2. The CO selectivity of Rh/MCM-41 reached 0.82. Here, we compare our CO selectivity for plastic gasification with the previous reports using photocatalysts. Ohtani *et al.* reported the CO/CO_2 ratio of 0.28 using the LDPE film mixed with TiO_2,[34] and Nabi *et al.* reported the CO/CO_2 ratio of 0.21 using a polystyrene–TiO_2 slurry system.[49] While the experimental conditions of these previous studies were different from the present study, our Rh/MCM-41 system leads high CO selectivity. In the present study, the CO selectivity trend in the case of LDPE decomposition was similar to the case of liquid C_8H_{18}, but there were some differences. The generation of CH_4, C_2H_4 and C_2H_6 was limited in the case of the LDPE degradation by Rh/MCM-41. We suppose that the shorter chain in liquid C_8H_{18} induces more gaseous hydrocarbons since chain scission at the edge part is more likely to occur. There are more chain edges in liquid C_8H_{18} as compared to LDPE. The stability of Rh/$SrTiO_3$ under simultaneous bandgap excitation and photothermal conditions has been demonstrated previously,[42] suggesting that the catalyst structure is maintained under the present reaction conditions.

4. Conclusions

We elucidated the difference between Rh/$SrTiO_3$ and Rh/MCM-41 for the degradation of hydrocarbons. Rh/MCM-41 exhibited higher selectivity toward CO production over CO_2 under the degradation experiment using liquid alkane (C_8H_{18}). The different product trend between Rh/$SrTiO_3$ and Rh/MCM-41 is attributed to the oxidizing power of the catalysts, as suggested by liquid-phase analysis conducted using GC-MS. In addition to the degradation of C_8H_{18}, we examined the LDPE degradation by Rh/$SrTiO_3$ and Rh/MCM-41, and the produced gas trends were consistent with those of the results using C_8H_{18}. The present findings are informative for using photon energy toward plastic waste degradation, which upconverts polyolefins to valuable chemicals like syngas.

Conflicts of interest

There are no conflicts to declare.

Data availability

The data supporting this article have been included as part of the supplementary information (SI). supplementary information is available. See DOI: https://doi.org/10.1039/d6se00038j.

Acknowledgements

This study was partially supported by JSPS KAKENHI (grant numbers 23H02042, 23K26735, 23K17953, and 25KJ1275).

References

1 J. Sun, J. Dong, L. Gao, Y. Q. Zhao, H. Moon and S. L. Scott, *Chem. Rev.*, 2024, **124**, 9457–9579.
2 K. Faust, P. Denifl and M. Hapke, *ChemCatChem*, 2023, **15**, e202300310.
3 C. Kassargy, S. Awad, G. Burnens, K. Kahine and M. Tazerout, *J. Anal. Appl. Pyrolysis*, 2017, **127**, 31–37.
4 G. Elordi, M. Olazar, G. Lopez, M. Artetxe and J. Bilbao, *Ind. Eng. Chem. Res.*, 2011, **50**, 6061–6070.
5 A. I. Eldahshory, K. Emara, M. S. Abd-Elhady and M. A. Ismail, *Sci. Rep.*, 2023, **13**(1), 1–12.
6 S. Rahimi, A. Shahdadi, R. Alizadeh and M. Rostamizadeh, *J. Taiwan Inst. Chem. Eng.*, 2025, **173**, 106184.
7 A. Koti, P. Khongprom and S. Ratanawilai, *ACS Omega*, 2025, **10**, 5744–5755.
8 H. Wang, M. van Akker, J. G. M. Winkelman, A. Heeres and H. J. Heeres, *Energy Fuels*, 2025, **39**, 3564–3574.
9 G. Lopez, M. Artetxe, M. Amutio, J. Alvarez, J. Bilbao and M. Olazar, *Renewable Sustainable Energy Rev.*, 2018, **82**, 576–596.
10 S. K. Sansaniwal, K. Pal, M. A. Rosen and S. K. Tyagi, *Renew. Sustain. Energy Rev.*, 2017, **72**, 363–384.
11 J. A. Sancho, M. P. Aznar and J. M. Toledo, *Ind. Eng. Chem. Res.*, 2008, **47**, 1005–1010.
12 U. Arena and F. Di Gregorio, *Energy*, 2014, **68**, 735–743.
13 V. Wilk and H. Hofbauer, *Fuel*, 2013, **107**, 787–799.
14 A. Erkiaga, G. Lopez, M. Amutio, J. Bilbao and M. Olazar, *Fuel*, 2013, **109**, 461–469.
15 G. Ruoppolo, P. Ammendola, R. Chirone and F. Miccio, *Waste Manage.*, 2012, **32**, 724–732.
16 F. Pinto, C. Franco, R. N. Andre, M. Miranda, I. Gulyurtlu and I. Cabrita, *Fuel*, 2002, **81**, 291–297.
17 I. Barbarias, G. Lopez, J. Alvarez, M. Artetxe, A. Arregi, J. Bilbao and M. Olazar, *Chem. Eng. J.*, 2016, **296**, 191–198.
18 U. Arena, L. Zaccariello and M. L. Mastellone, *Waste Manage.*, 2010, **30**, 1212–1219.
19 G. Sharma, A. K. Dewangan, A. K. Yadav and A. Ahmad, *J. Therm. Anal. Calorim.*, 2024, **149**(23), 13629–13651.
20 S. Chu, B. Zhang, X. Zhao, H. Sen Soo, F. Wang, R. Xiao and H. Zhang, *Adv. Energy Mater.*, 2022, **12**, 2200435, DOI: 10.1002/aenm.202200435.

21 J. Lin, K. Hu, Y. Wang, W. Tian, T. Hall, X. Duan, H. Sun, H. Zhang, E. Cortés and S. Wang, *Nat. Commun.*, 2024, **15**, 8769, DOI: 10.1038/s41467-024-53055-1.
22 Y. He, A. U. Rehman, M. Xu, C. A. Not, A. M. C. Ng and A. B. Djurišić, *Heliyon*, 2023, **9**, e22562, DOI: 10.1016/j.heliyon.2023.e22562.
23 J. Jeyaraj, V. Baskaralingam, T. Stalin and I. Muthuvel, *Environ. Res.*, 2023, **233**, 116366, DOI: 10.1016/j.envres.2023.116366.
24 R. Jiang, G. Lu, Z. Yan, J. Liu, D. Wu and Y. Wang, *J. Hazard. Mater.*, 2021, **405**, 124247, DOI: 10.1016/j.jhazmat.2020.124247.
25 J. He, L. Han, W. Ma, L. Chen, C. Ma, C. Xu and Z. Yang, *iScience*, 2023, **26**, 106833.
26 A. Severino, A. Grirrane, M. Cabrero-Antonino, C. Lavorato, P. Argurio, R. Molinari and H. García, *ACS Appl. Nano Mater.*, 2025, **8**, 14720–14732.
27 G. Zhou, H. Xu, H. Song, J. Yi, X. Wang, Z. Chen and X. Zhu, *ACS Catal.*, 2024, **14**, 8694–8719.
28 R. Verma, S. Singh, M. K. Dalai, M. Saravanan, V. V. Agrawal and A. K. Srivastava, *Mater. Des.*, 2017, **133**, 10–18.
29 R. T. Thomas, V. Nair and N. Sandhyarani, *Colloids Surf., A*, 2013, **422**, 1–9.
30 X. u. Zhao, Z. Li, Y. Chen, L. Shi and Y. Zhu, *J. Mol. Catal. A:Chem.*, 2007, **268**, 101–106.
31 W. Asghar, I. A. Qazi, H. Ilyas, A. A. Khan, M. A. Awan and M. Rizwan Aslam, *J. Nanomater.*, 2011, **2011**, 461930.
32 T. Xu, T. Shan, Y. Jiang, L. hua Xu, H. Zhang and S. Chu, *ChemSusChem*, 2025, **18**, e202402310.
33 J. Xu, X. Jiao, K. Zheng, W. Shao, S. Zhu, X. Li, J. Zhu, Y. Pan, Y. Sun and Y. Xie, *Natl. Sci. Rev.*, 2022, **9**, nwac011.
34 B. Ohtani, S. Adzuma, S.-I. Nishimoto and T. Kagiya, *Polym. Degrad. Stab.*, 1992, **35**, 53–60.
35 Y. Liu, C. Li, H. Yu and J. Guo, *Chem*, 2022, **8**, 2586–2588.
36 C. Xing, H. Cai, D. Kang and W. Sun, *Adv. Energy Sustain. Res.*, 2023, **4**, 2300015.
37 C. Xing, C. Mao, S. Wang, Y. Zhou, L. Wu, D. Zhang, D. Kang, D. Yang, W. Gong, W. Wei, L. Wang, C. Li, G. A. Ozin, D. Yang and W. Sun, *Nat. Catal.*, 2025, **8**(6), 556–568.
38 H. Luo, D. Yao, K. Zeng, J. Li, S. Yan, D. Zhong, J. Hu, H. Yang and H. Chen, *Fuel Process. Technol.*, 2022, **230**, 107205.
39 Y. Miao, Y. Zhao, G. I. N. Waterhouse, R. Shi, L. Z. Wu and T. Zhang, *Nat. Commun.*, 2023, **14**(1), 1–10.
40 H. Kaneko, S. Shoji, Y. Cho, T. Sugimura, A. Hashimoto, H. Abe, A. Yamaguchi and M. Miyauchi, *Green Chem.*, 2025, **27**, 15056–15060.
41 T. Takata, J. Jiang, Y. Sakata, M. Nakabayashi, N. Shibata, V. Nandal, K. Seki, T. Hisatomi and K. Domen, *Nature*, 2020, **581**(7809), 411–414.
42 S. Shoji, X. Peng, A. Yamaguchi, R. Watanabe, C. Fukuhara, Y. Cho, T. Yamamoto, S. Matsumura, M. W. Yu, S. Ishii, T. Fujita, H. Abe and M. Miyauchi, *Nat. Catal.*, 2020, **3**(2), 148–153.
43 H. Kaneko, Y. Cho, T. Sugimura, A. Hashimoto, A. Yamaguchi and M. Miyauchi, *Chem. Commun.*, 2024, **60**, 10406–10409.
44 H. Jiang, X. Peng, A. Yamaguchi, T. Fujita, H. Abe and M. Miyauchi, *Chem. Commun.*, 2019, **55**, 13765–13768.
45 S. Brunauer, P. H. Emmett and E. Teller, *J. Am. Chem. Soc.*, 1938, **60**, 309–319.
46 F. Gugumus, *Polym. Degrad. Stab.*, 2000, **67**, 35–47.
47 P. Y. Lu, L. A. Ningsih, A. C. Heksa, C. C. Hu, W. C. Chen and Y. C. Chiu, *Polym. J.*, 2025, **57**(5), 575–586.
48 A. M. Watson, X. Zhang, R. Alcaraz De La Osa, J. M. Sanz, F. González, F. Moreno, G. Finkelstein, J. Liu and H. O. Everitt, *Nano Lett.*, 2015, **15**, 1095–1100.
49 I. Nabi, A. U. R. Bacha, K. Li, H. Cheng, T. Wang, Y. Liu, S. Ajmal, Y. Yang, Y. Feng and L. Zhang, *iScience*, 2020, **23**, 101326.